New analytical parameters for B2 phase prediction as a complement to multiclass phase prediction using machine learning in multicomponent alloys: A computational approach with experimental validation

Angelo Oñate, Herrim Seidou, Jérome Tchoufang-Tchuindjang, Víctor Tuninetti, Alejandra Miranda, Juan Pablo Sanhueza, Anne Mertens

PII: S0925-8388(25)01508-7

DOI: https://doi.org/10.1016/j.jallcom.2025.179950

Reference: JALCOM179950

To appear in: *Journal of Alloys and Compounds*

Received date: 4 February 2025
Revised date: 17 March 2025
Accepted date: 19 March 2025

Please cite this article as: Angelo Oñate, Herrim Seidou, Jérome Tchoufang-Tchuindjang, Víctor Tuninetti, Alejandra Miranda, Juan Pablo Sanhueza and Anne Mertens, New analytical parameters for B2 phase prediction as a complement to multiclass phase prediction using machine learning in multicomponent alloys: A computational approach with experimental validation, *Journal of Alloys and Compounds,* (2025) doi:https://doi.org/10.1016/j.jallcom.2025.179950

New analytical parameters for B2 phase prediction as a complement to multiclass phase prediction using machine learning in multicomponent alloys: A computational approach with experimental validation

Angelo Oñate[1,*], Herrim Seidou[2], Jérome Tchoufang-Tchuindjang[2], Víctor Tuninetti[3], Alejandra Miranda[4] Juan Pablo Sanhueza[1], Anne Mertens[2,*]

[1]Department of Materials Engineering, Faculty of Engineering, Universidad de Concepción, Edmundo Larenas 315, Concepción, Chile

[2]Metallic Materials Science (MMS), A&M Department, University of Liège, Liège, 4000, Belgium

[3]Department of Mechanical Engineering, Faculty of Engineering, Universidad de La Frontera, Francisco Salazar 01145, Temuco, Chile

[4]Doctorado en Ingeniería, Facultad de Ingeniería, Universidad de Concepción, Edmundo Larenas 219, Concepción, Chile

Corresponding authors *: Angelo Oñate: aonates@udec.cl; Anne Mertens: anne.Mertens@uliege.be

Abstract

Accurate phase prediction in multicomponent alloys is challenging due to the complex interactions among different microstructural phases, especially in alloys with both face-centered cubic (FCC) and body-centered cubic (BCC) structures. This challenge is further intensified by the presence of secondary intermetallic phases, such as the ordered BCC (B2) phase, which improves the mechanical properties but is difficult to distinguish from the disordered BCC phase. Current predictive models rely primarily on the valence electron concentration (VEC), which is useful but fails to effectively distinguish the B2 phase in different alloy systems. This study introduces a novel machine learning-based predictive framework, which was validated through exploratory data analysis, CALPHAD simulations, and experimental results. It incorporates three analytical descriptors for SOHEI B2 phase prediction in the FCC, BCC, and FCC+BCC systems. By integrating the atomic radius difference (δr), valence electron concentration (VEC), and shear modulus (G), this approach enhances the accuracy of B2 phase classification in high-entropy alloys. Furthermore, a combined machine learning model integrating random forest (RF) and eXtreme Gradient Boosting (XGBoost) achieved 77% accuracy, significantly improving FCC+BCC+IM phase prediction from 25% to 62.5%. The

most relevant findings suggest that the FCC+B2 system remains stable for δr > 5.23%, the BCC+B2 system is stable for VEC > 6.4, and the FCC+BCC+B2 system is stable for G > 68.22 GPa. This work represents a significant advancement in the design of multicomponent alloys that require the SOHEI B2 phase as a reinforcement mechanism, providing a data-driven and experimentally validated approach.

Keywords:

Machine learning; Multicomponent alloys; Multiclass classification; SOHEI B2 phase stability; CALPHAD

1. Introduction

The development of alloys that achieve an optimal balance between mechanical strength and ductility is of significant interest. Alloys with face-centered cubic (FCC) and body-centered cubic (BCC) microstructures are particularly attractive because of their inherent ability to maintain this balance. Moreover, these alloys must be lightweight, as this characteristic reduces dead loads in structural applications and facilitates weight reduction in maritime, terrestrial, and aerospace vehicles, thereby increasing fuel efficiency. Furthermore, when the microstructural configuration is compositionally well designed, it can provide excellent corrosion resistance, expanding the range of applications and improving the material's functional performance [1].

In recent years, multicomponent alloys have attracted significant interest because of their extensive configurational flexibility and the challenges associated with alloy design, given their broad and complex compositional landscape. In the context of FCC+BCC microstructure alloys, eutectic high-entropy alloys (EHEAs) have emerged as high-performance materials [2,3], providing mechanical reinforcement through the ordered BCC (B2) phase [4]. These EHEAs stand out due to their combination of high mechanical strength and excellent castability, bridging the gap toward industrial

scalability [3]. Their remarkable potential extends to applications in welding, surface engineering, and additive manufacturing, making them highly versatile for advanced engineering solutions.

Microstructural control of these alloys is crucial to optimizing their performance. For example, Lin et al. [5] investigated the effect of lanthanum microalloying on the microstructure and electrochemical properties of the $AlCoCrFeNi_{2.1}$ eutectic high-entropy alloy (EHEA) under simulated proton exchange membrane fuel cell (PEMFC) conditions. The results revealed that the alloy without lanthanum exhibited a eutectic microstructure composed of a high-strength BCC phase (NiAl) and a high-ductility FCC phase (CoCrFe) with superior corrosion resistance. However, adding lanthanum promotes BCC phase stabilization, thereby reducing corrosion resistance. These findings demonstrate the necessity of achieving an optimized design for these alloys, which combine high aluminum and chromium contents to ensure excellent corrosion resistance [6], highlighting the significant potential of EHEAs for industrial applications.

Z.J. Shi et al. [7] investigated the corrosion resistance of the Al0.3CoCrFeNi alloy and observed the formation of a B2 phase enriched in Al and Ni. This phase was identified in samples annealed at temperatures between 800 °C and 900 °C, appearing as rod-shaped precipitates distributed along grain boundaries and within the grains. However, these precipitates disappeared when the temperature increased to 1000 °C. A greater fraction of the B2 phase in the microstructure reduced corrosion resistance, as this phase serves as a preferential nucleation site for pitting corrosion. This behavior is attributed to the increased reactivity resulting from the elevated Al content and the reduced Cr content in the B2 phase.

These findings are consistent with previous studies demonstrating that the B2 phase serves as a preferential site for pitting corrosion [7,8]. Specifically, L. Song et al. [8], who studied a eutectic AlCoCrFeNi2.1 alloy fabricated via vacuum melting featuring an FCC/BCC/B2 structure. Their study demonstrated that the alloy's passive film remains stable in sulfuric acid solutions at low temperatures. Furthermore, temperature variations were found to influence the hydroxide-to-oxide ratios of Fe and

Cr without significantly affecting the contents of Al and Ni, which are key factors in the passive behavior of the alloy. The corrosion in this EHEA predominantly occurs in the B2 phase, which is rich in Al and Ni, manifesting as pitting corrosion, the primary form of degradation at low temperatures. This behavior highlights the potential of these alloys for industrial environments where corrosion resistance is critical, a conclusion also supported by Wu et al. [9].

From a mechanical perspective, the B2 phase is critical in strengthening high-entropy alloys while maintaining ductility control. This is achieved through FCC/B2 interfaces, which act as effective barriers to dislocation motion, thereby increasing the mechanical strength. This is supported by the work of Zhang et al. [10], who analyzed the submicron mechanical response of an $AlCoCrFeNi_{2.1}$ eutectic alloy via nanoindentation. Their results demonstrated that the FCC phase exhibits greater deformability due to higher dislocation activity compared to the B2 phase, indicating an increased activation rate of slip systems. This directly influences the co-deformation process and the balance between ductility and mechanical strength. Additionally, the B2 phase exhibits greater thermal stability than the FCC phase, thereby contributing to structural stability under thermal cycling and high-temperature conditions, such as those encountered in aerospace applications [11].

A study by Jiang et al. [12] on the $AlCoCrFeNi_{2.1}$ eutectic high-entropy alloy demonstrated that remelting and heat treatment at 1100°C for four hours significantly enhanced its mechanical properties. The ultimate tensile strength increased by 2.4%, reaching 1061 MPa, whereas the yield strength decreased by only 6.3%, stabilizing at 581 MPa. Moreover, ductility exhibited a remarkable 105% increase, achieving 24.8% fracture strain. The primary deformation mechanisms observed include the formation of slip lines in the FCC phase promoting plasticity, and the role of the B2 phase as a dislocation barrier, which enhances the tensile strength while minimizing the loss of yield strength.

Similar findings were reported by Zhang et al. [13] who investigated a eutectic high-entropy alloy with a core-shell structure, assessing its impact on mechanical properties. The microstructure

exhibited an FCC core, enhancing ductility, and a B2 shell, increasing rigidity and serving as a strengthening mechanism. Tensile testing revealed a yield strength of 680 MPa, an ultimate tensile strength of 1105 MPa, and a fracture strain of 28.5%. The FCC phase promotes plasticity through dislocation slip, while the B2 phase acts as a barrier to dislocation motion, optimizing the balance between strength and ductility.

The design of multicomponent alloys containing the B2 phase still face challenges, particularly in predicting its stability and formation. Machine learning offers a versatile approach to designing multicomponent alloys [14–19], addressing not only phase prediction but also the estimation of their functional properties, such as mechanical performance [20,21]. Typically, machine learning models focus on predicting solid solutions (SS), amorphous phases (AM), and intermetallics (IM), which often leads to overestimated results, thereby circumventing the challenges posed by phase overlap in complex systems with high mutual affinity [22–24]. Advancements in multiclass phase prediction for multicomponent alloys remain limited. This was demonstrated by Yan et al. [21], whose comprehensive review highlights that only a few studies address independent phase prediction, underscoring the need for further development in this area.

The B2 phase is characterized as an ordered phase, known as a structurally ordered high-entropy intermetallic (SOHEI), which maintains a balance between short-range disorder and long-range order. Additionally, it is a sought-after intermetallic for applications requiring a trade-off between strength and ductility [25]. Predicting the B2 phase in multicomponent alloys is particularly challenging due to its strong affinity with the BCC phase [26], which leads to minimal variations in thermochemical parameters compared to other intermetallics. Stability ranges for the B2 phase have been associated with VEC values between 6 and 7 [25]; however, this criterion does not apply to systems such as FCC and FCC+BCC, where stability ranges significantly overlap. Wang et al. [26] analyzed the challenge of predicting the B2 phase in multicomponent systems, focusing exclusively on BCC, FCC+BCC, and FCC systems using experimental results and machine learning. Their findings indicate that the

B2 phase typically forms in alloys containing elements with significant atomic size differences, as the BCC/B2 structure accommodates greater lattice distortion compared to the FCC phase. Additionally, for VEC < 6.87, the formation of BCC/B2 is favored, while in the range of 6.87 < VEC < 9.16, there is a higher probability of forming dual-phase BCC/B2+FCC alloys.

However, these results do not effectively distinguish the presence or absence of the B2 phase, as no clear distinction is made between B2 and other phases. This limitation arises from the overlapping effect of parameters such as VEC across different systems and the high affinity of B2 with the BCC phase. Moreover, in mixed-phase systems such as FCC+BCC, predicting the B2 phase becomes even more complex, as there is an inherent balance between the predictive parameters of the individual phases, leading to a greater challenge in phase classification.

These findings highlight the significant current difficulty in accurately predicting the B2 phase in multicomponent alloys—an intermetallic phase of great interest due to its beneficial contributions to material properties, such as enhancing strength without significantly compromising ductility and facilitating co-deformation processes in eutectic alloys [27]. However, in the absence of key predictive parameters to support machine learning results, efficiently designing multicomponent alloys incorporating the B2 phase remains impractical.

Based on the previous discussion, the effect of the FCC+BCC/B2 phase in multicomponent alloys is particularly significant, as the B2 phase acts as a mechanical reinforcement agent, while the FCC and BCC phases provide a balance between strength and ductility. For this reason, there is considerable interest in developing multicomponent alloys with the B2 phase. However, design strategies to stabilize this phase are still lacking, highlighting the need for new parameters to predict its stability and refine machine learning results. Notably, FCC+BCC eutectic alloys exhibit high mechanical performance due to the co-deformation capability between the primary phases, resulting in enhanced mechanical behavior.

This study aims to increase the phase prediction accuracy of the multicategorical machine learning approach by implementing an ensemble technique to improve the identification of FCC+BCC+IM phases and optimize the prediction of the B2 phase in multicomponent systems. This is achieved by incorporating new independent predictive parameters for FCC+B2, BCC+B2, and FCC+BCC+B2 systems, thereby mitigating overlapping effects and subcategorization issues. These improvements will enable the effective design of multicomponent alloys that require the incorporation of the B2 phase. To accomplish this, machine learning models—including support vector machine (SVM), XGBoost, and random forest—will be evaluated on a dataset comprising 2591 experimental results. Furthermore, exploratory data analysis (EDA) was performed on 237 experimental phase data points across various microstructural categories (FCC, FCC+B2, BCC, BCC+B2, FCC+BCC, FCC+BCC+B2) to identify complementary predictive parameters for the B2 phase. This approach will refine the machine learning predictions, ensuring a more accurate and efficient prediction of the B2 phase in multicomponent systems. The machine learning and exploratory data analysis results will be applied to six multicomponent alloys and validated through computational CALPHAD simulations, as well as experimental validation using differential thermal analysis (DTA), scanning electron microscopy (SEM), and electron backscatter diffraction (EBSD).

2. Methodology

A supervised multicategorical machine learning model, based on VEC, δHmix, and δX, was applied following the methodology of Oñate et al. [28], employing support vector machine, eXtreme gradient boosting, and random forest models trained on a dataset of 2591 data points [29,30]. These data points were categorized as follows: FCC (496), BCC (617), hexagonal close-packed (HCP) (72), BCC+HCP (85), BCC+FCC (197), FCC+IM (277), BCC+IM (205), FCC+BCC+IM (76), IM (368), and amorphous (AM) (198). Additionally, CALPHAD simulations with the SSOL8 database in Thermo-Calc were used to generate phase diagrams, indicating phase stability under atmospheric pressure by minimizing Gibbs free energy.

The classification metrics were evaluated in terms of accuracy, precision, recall, F1 score, and ROC AUC. A detailed description of each metric is provided below.

Accuracy measured the proportion of correctly classified instances relative to the total number of evaluated instances. This was computed via Equation (1):

$$Accuracy = \frac{TP + TN}{TP + TN + FP + FN} x100 \qquad (1)$$

Where TP represents true positives, TN true negatives, FP false positives, and FN false negatives.

Precision indicated the proportion of positive predictions that were truly correct. This was calculated according to Equation (2):

$$Precision = \frac{TP}{TP + FP} x100 \qquad (2)$$

Recall measured the model's ability to correctly identify positive instances. It was calculated according to Equation (3):

$$Recall = \frac{TP}{TP + FN} x100 \qquad (3)$$

The F1 score was the harmonic means of precision and recall, providing a balanced performance measure. It was calculated according to Equation (4):

$$F1 - score = 2x \frac{PrecisionxRecall}{Precision + Recall} \qquad (4)$$

The ROC AUC was the area under the Receiver Operating Characteristic (ROC) curve, which evaluated the model's ability to distinguish between classes.

The support vector machine (SVM) model is a kernel-based algorithm that identifies the optimal hyperplane for class separation in high-dimensional spaces. It was particularly useful in scenarios with complex decision boundaries. The SVM was configured with a label encoder to transform phase-

related data into numerical values, facilitating their use as classification labels. Phase classification parameters were grouped into the input variable **X**, while phase data were assigned to the response variable **Y**. Grid search optimization was employed to tune the hyperparameters, exploring **C** values between 0.1 and 10 to balance broad margins with data fit. Additionally, γ values between 0.001 and 1 were investigated to enhance the model's sensitivity to local patterns. The dataset was split into 80% training and 20% testing sets. A 10-fold cross-validation with randomized partitions was conducted to ensure data representativeness. To address class imbalance, no class weight adjustments were applied in the SVM, as its optimization function inherently maximizes the margin between classes, reducing the impact of imbalance. However, alternative strategies, such as adjusting the C parameter, have been explored to mitigate bias toward majority classes. During cross-validation, accuracy was the primary evaluation criterion, while F1 score, recall, and precision provided additional insights into minority classification.

Random Forest is an ensemble learning technique that builds multiple decision trees and aggregates their outputs using a bagging approach, improving accuracy and reducing overfitting. A grid search optimization was conducted to fine-tune key hyperparameters in the random forest model, enhancing its predictive capacity. The number of trees in the forest was adjusted by evaluating values between 100 and 500. The optimal depth was configured with a minimum depth of 10 and increments of 20 levels, enabling the model to capture complex patterns. To address class imbalance, class-weight adjustments were applied. Model validation was subsequently conducted using stratified 10-fold cross-validation to ensure the representativeness of all classes in each fold.

XGBoost is an optimized gradient-boosting framework that enhances predictive performance by sequentially training weak learners (decision trees) using gradient descent-based optimization. It applies regularization and shrinkage techniques to mitigate overfitting. For the XGBoost model, hyperparameter optimization included tuning the learning rate within a range of 0.01 to 0.2 and controlling the learning process speed during training. The maximum tree depth was limited to 10

levels with increments of 20, allowing the model to capture complex data relationships. To address the class imbalance, class-weight adjustments were applied. Validation was performed using stratified 10-fold cross-validation to ensure the representativeness of all classes in each partition.

A soft voting classifier was implemented, combining the two best-performing models. Soft voting was used, leveraging probability outputs from each base model instead of discrete predictions. This approach improved the robustness of the ensemble model's decision-making.

For sample fabrication, high-purity elemental powders supplied by abcr GmbH (Germany) were used. Thermal analysis was subsequently conducted using a NETZSCH STA 449C Jupiter DTA system. Approximately 700 mg of powder mixture was prepared for each DTA test. To ensure near-equilibrium solidification and enable cross-comparison of the results, the heating and cooling rates were consistently maintained at 5°C/min. The samples were heated to 1550°C in Al_2O_3 crucibles within an argon-purged chamber to minimize oxygen levels. An essential reference measurement involved an empty crucible subjected to the same temperature profile, eliminating any artificial signals originating from the sample holder.

The samples were subsequently polished for microstructural observation under an optical microscope (OM) and further analyzed using a Tescan Clara ultra-high-resolution scanning electron microscope (SEM). The samples were chemically etched with 3% nital. Phases and crystallographic analysis were performed using electron backscatter diffraction (EBSD).

Exploratory data analysis (EDA) was performed in Python on a dataset of 237 experimentally validated phase compositions classified into FCC, FCC+B2, BCC, BCC+B2, FCC+BCC, and FCC+BCC+B2 categories. A cross-analysis approach was employed, considering predictive parameters such as the mixing enthalpy difference, valence electron concentration, and atomic radius difference. This analysis was conducted to identify predictive parameters for the B2 phase across the

three different phase categories, complementing machine learning results and enabling the effective design of functional alloys requiring the B2 phase.

The analytical calculations of the physical and thermodynamic parameters are described by the following equations, which were executed in the Jupyter Notebook and computed for the chemical compositions of each sample.

Equation (5) is used to calculate the atomic radius difference in the alloys, Δr.

$$\Delta r = \sqrt{\sum_{i=1}^{n} x_i \left(1 - \frac{r_i}{r}\right)^2} \qquad (5)$$

where x_i is the concentration of element i in the alloy and r_i is the atomic radius of the ith component.

Equation (6) represents the mixing enthalpy of the alloy ΔH_{mix}, which describes the chemical interactions between its constituents.

$$\Delta H_{mix} = \sum_{j \neq i}^{n} \sum_{i=1}^{n} 4 \Delta H_{ij}^{m} x_i x_j \qquad (6)$$

where ΔH_{ij}^{m} is the mixing enthalpy of the ij pair.

The mixing enthalpy ΔS_{mix} is described as the configurational enthalpy, as shown in Equation (7).

$$\Delta S_{mix} = -R \sum_{i=1}^{n} x_i ln x_i \qquad (7)$$

where R corresponds to the ideal gas constant.

The parameter Ω reflects the competition between the driving force for solid solution formation and the driving force for the formation of intermetallics or elemental segregation, as described in Equation (8).

$$\Omega = \frac{T_m \Delta S_{mix}}{|\Delta H_{mix}|} \qquad (8)$$

where Tm is the melting temperature of the multicomponent system.

The ΔVEC parameter describes the difference in the valence electron concentration of the system and is defined by Equation (9).

$$\Delta VEC = \sqrt{\sum_{i=1}^{n} x_i (VEC - VEC_i)^2} \qquad (9)$$

where VEC_i corresponds to the valence electron concentration of the i^{th} component.

One of the most relevant parameters in multicomponent alloys for describing phase stability is the atomic packing factor γ, which quantifies the lattice distortion of the multicomponent alloy. This parameter is defined by Equation (10).

$$\gamma = \frac{\left(1 - \sqrt{\frac{(\mathrm{r_s} + \bar{r})^2 - \bar{r}^2}{(\mathrm{r_s} + \bar{r})^2}}\right)}{\left(1 - \sqrt{\frac{(\mathrm{r_L} + \bar{r})^2 - \bar{r}^2}{(\mathrm{r_L} + \bar{r})^2}}\right)} \qquad (10)$$

where r_L and r_s represent the radii of the largest and smallest atoms in the compositional system, respectively.

Equation (11) describes the electronegativity mismatch $\Delta\chi^P$ using the Pauling scale.

$$\Delta\chi^P = \sqrt{\sum_{i=1}^{n} x_i (\chi^P - \chi_i^P)^2} \qquad (11)$$

where χ_i^P corresponds to the electronegativity of the i^{th} component.

The parameter describing the number of itinerant electrons per atom (e/a) is determined using equation (12):

$$e/a = \sum_{i=1}^{n} x_i (e/a)_i \qquad (12)$$

where $(e/a)_i$ corresponds to the number of itinerant valence electrons per atom of the i[th] component.

The shear modulus G of the multicomponent alloy is calculated using Equation (13):

$$G = \sum_{i=1}^{n} x_i G_i \qquad (13)$$

where G_i corresponds to the shear modulus of the i[th] component.

Similarly, the shear modulus difference of the multicomponent system ΔG can be determined using Equation (14):

$$\Delta G = \sum_{i=1}^{n} x_i \left(1 - \frac{G_i}{G}\right)^2 \qquad (14)$$

The chemical composition of the obtained samples and the results of the parameters described in Equations (5) through (14) are presented in Table 1, where two groups of alloys can be distinguished: the first group is devoid of Al, and the second group contains Al. The choice of these alloys was part of a previous work in which DTA was used as a tool for prescreening compositions suitable to design corrosion-resistant alloys for laser powder bed fusion (LPBF) [31].

Table 1. Summary of the two groups of fabricated multicomponent alloys.

Alloys	δr [%]	δHmix [kJ/mol]	δSmix [J/molK]	Ω	VEC	γ	δX	e/a	G [GPa]	δG
CrFeMnNi	3.57	-4.00	11.52	5.21	7.75	1.095	0.14	1.75	87.75	0.033
Cr2Fe2MnNi	3.10	-2.88	11.05	7.16	7.50	1.095	0.12	1.67	91.33	0.034
CrFe2MnNi2	3.12	-4.22	11.05	4.70	8.16	1.095	0.13	1.83	84.83	0.026
AlCrFeMnNi	5.82	-12.48	13.38	1.75	6.80	1.167	0.13	2.00	75.40	0.143
AlCrFe2MnNi2	5.42	-10.86	12.88	1.98	7.42	1.168	0.13	2.00	76.42	0.100
AlCrFe2Ni2	5.47	-11.11	11.05	1.69	7.49	1.169	0.11	2.17	76.16	0.118

3. Analysis and Results

3.1. Computational simulation

The correlation study indicates that the phase class positively correlates with the VEC, which is associated with its influence on phase prediction (see Figure 1). This finding demonstrates that the valence electron concentration has a global impact on phase prediction in multicomponent alloys, transcending the subcategorization of phases and their configurations (FCC, BCC, HCP, IM, AM). In contrast, the valence electron difference and mixing enthalpy do not contribute globally to phase prediction. This confirms that the VEC is the primary predictor in multicomponent alloys and validates the method employed by Oñate et al. [28].

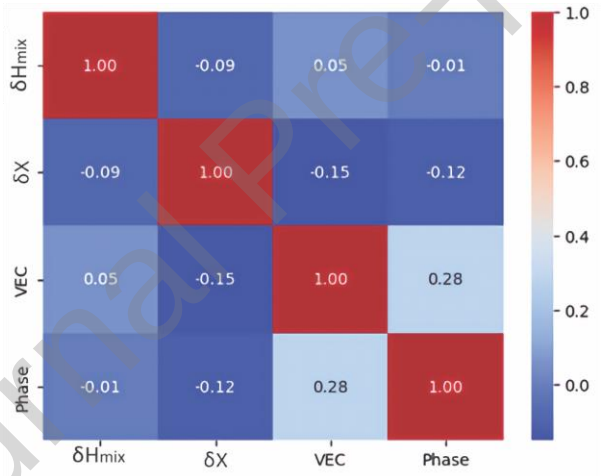

Figure 1. Correlation matrix of descriptors used for phase prediction via machine learning.

Figure 2 presents the confusion matrices obtained for the three models analyzed. Figure 2.a shows that the SVM model performs better in predicting the BCC+HCP phase than the XGBoost and random forest models. However, the SVM model demonstrates no predictive capability for the FCC+BCC+IM phase, misclassifying this category as FCC+BCC, FCC+IM, or BCC during the prediction process. Figure 2.b displays the confusion matrix for the XGBoost model, which exhibits a higher overall prediction accuracy than the SVM model. However, the XGBoost model predicts the BCC+HCP phase 12.5% less accurately than the SVM model. For the FCC+BCC+IM phase, the

XGBoost model achieves a prediction rate of 25%, with the remaining predictions distributed as 18.75% for FCC+BCC and 37.5% for BCC. Figure 2.c shows the confusion matrix for the random forest model, which achieves a global prediction rate comparable to that of the XGBoost model but with higher accuracy in predicting FCC and BCC phases. The results highlight significant challenges in predicting the FCC+BCC+IM phase, a trend also observed in the predictive models by Oñate et al. [28]. This difficulty is strongly associated with the substantial overlap in classification parameters and the affinity between the BCC phase and the B2 intermetallic phase, which prevents clear separation between classes.

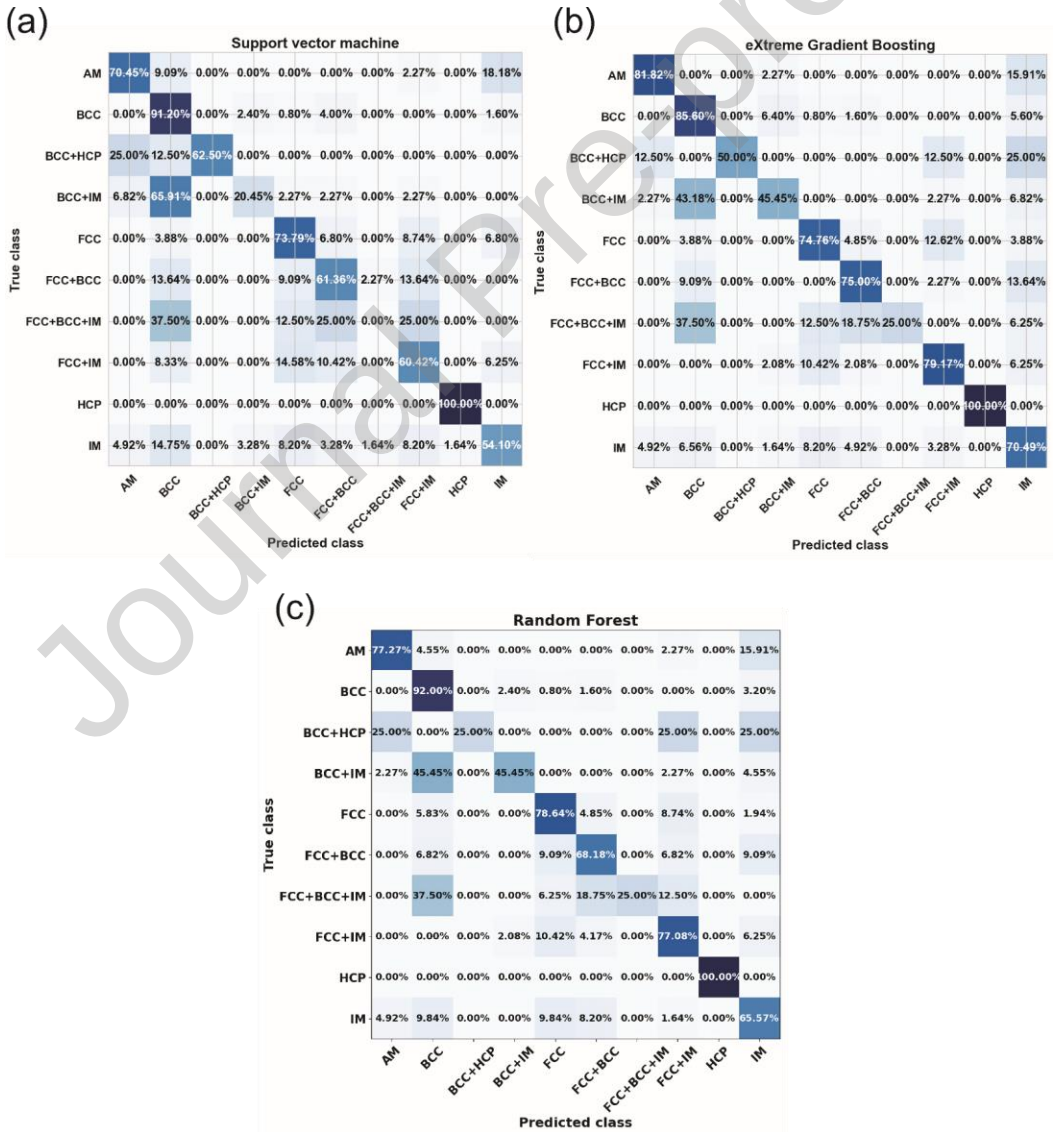

Figure 2. Confusion matrices for each classification model implemented in phase prediction: (a) support vector machine; (b) eXtreme gradient boosting; (c) random forest

The evaluation metrics results for the classification models implemented in machine learning are presented in Table 2. The random forest model achieved the highest number of correct predictions, with an accuracy of 75%. In terms of precision, the random forest method also recorded the highest number of true positives, followed by the XGBoost model. The random forest and XGBoost models achieved 74% recall, indicating their strong ability to detect positive instances. Regarding the F1 score, both the XGBoost and random forest demonstrated excellent balance in handling data imbalance, achieving good equilibrium between precision and recall. Finally, the XGBoost and random forest models exhibited significant class discrimination capabilities in terms of the ROC AUC. Based on these results, the best-performing model for phase prediction is the random forest. However, a significant challenge remains in accurately identifying the FCC+BCC+IM and FCC+BCC phases. For this reason, recent machine learning studies on phase prediction in multicomponent alloys emphasize the need to separate FCC+BCC from FCC+BCC+IM groups to achieve high prediction accuracy. An example of this approach is the work of Zhang et al. [32], who categorized prediction groups into solid solution phases (FCC, BCC, and FCC+BCC) and mixed phases with intermetallics (FCC+IM, BCC+IM, and FCC+BCC+IM). This classification strategy significantly improved phase prediction accuracy.

It is important to highlight that when FCC+BCC mixed phases form, commonly used physicochemical and electronic parameters as predictors tend to balance the primary phases in the alloy (FCC and BCC), leading to high levels of overlap [33]. Moreover, the presence of intermetallic phases can significantly affect key predictive parameters, such as atomic radius and valence electron concentration.

Zhang et al. [34], also discuss this issue, noting that the BCC+FCC phase often causes considerable misclassification with the individual BCC and FCC phases. This phenomenon extends to the

FCC+BCC+IM phase due to the variation in valence electron concentration induced by the independent presence of FCC and BCC phases in the system. Consequently, the addition of the IM phase introduces a noticeable variation proportional to the fraction of FCC and BCC phases and the type and volume fraction of the intermetallic phase present.

Table 2. Evaluation metrics for classification models in phase prediction.

Models	Accuracy (%)	Precision (%)	F1 score (%)	Recall (%)	ROC AUC (%)
SVM	**66**	**65**	**64**	**66**	**92**
XGBoost	**74**	**75**	**73**	**74**	**96**
Random Forest	**75**	**76**	**73**	**74**	**96**

Figure 3 illustrates the importance of the predictors used in phase prediction via the random forest model. The most significant predictor is the VEC, followed by the mixing enthalpy and, finally, the Pauling electronegativity. These results underscore the critical role of the valence electron concentration in phase prediction for multicomponent alloys, corroborating findings reported in various studies.

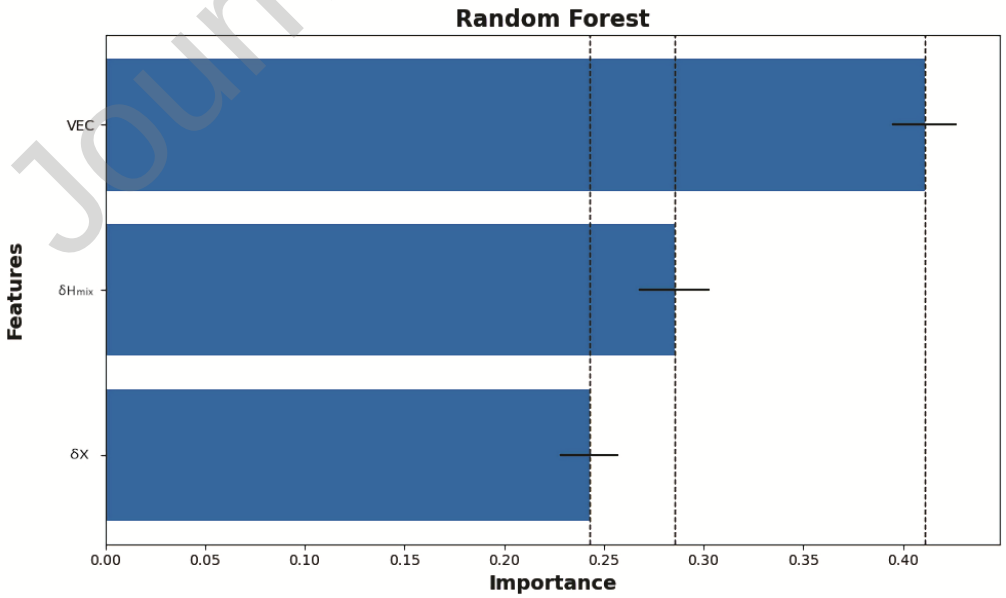

Figure 3. Permutation results for the random forest model among its classifiers.

To enhance the prediction performance of the classifiers, an ensemble was implemented between the XGBoost and random forest models. This approach aimed to improve the prediction and classification of the most complex phases, such as HCP+BCC, FCC+BCC+IM, and BCC+IM, which exhibit a high level of overlap in their predictors. Figure 4 presents the confusion matrix for the ensemble, which shows an improved ability to predict the most complex phases compared with the individual models. This enhancement resulted in a better prediction balance for each phase. The ensemble achieved an accuracy of 77%, which is 2.67% higher than that of the standalone random forest model.

The results obtained in this study outperform those reported by Oñate et al. [28] for the random forest model in multiclass phase classification by 2.93%. A summary of the evaluation metrics for the ensemble is presented in Table 3.

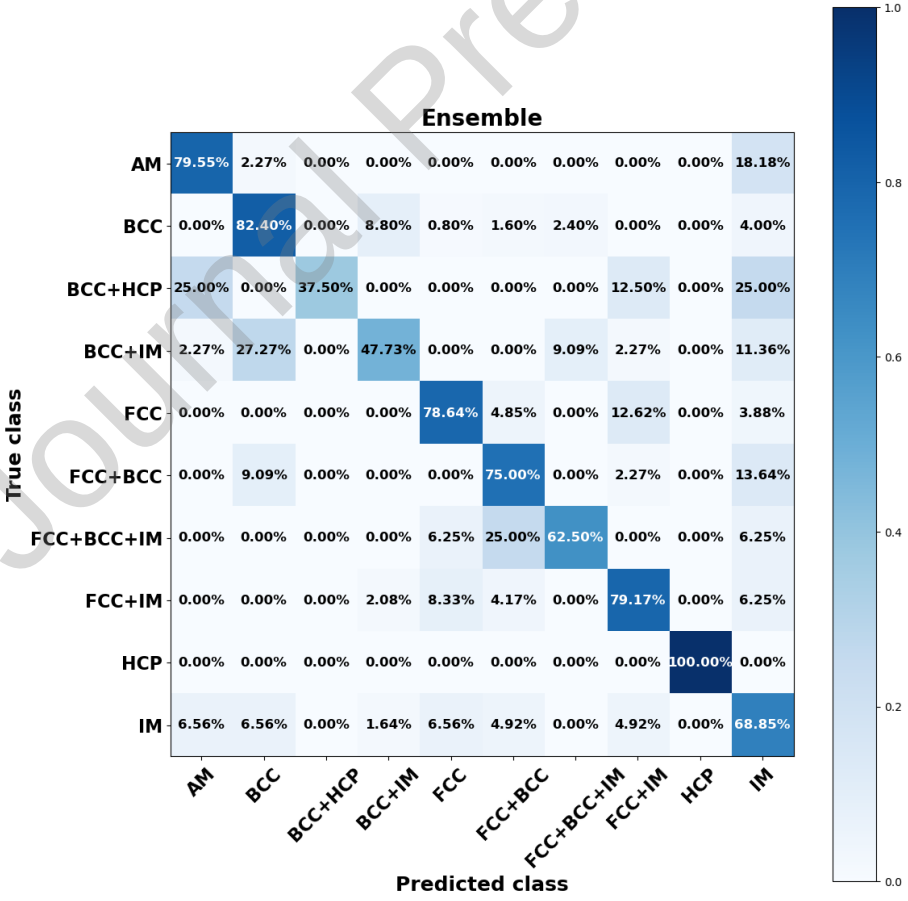

Figure 4. Confusion matrix for the ensemble of random forest and XGBoost models.

Table 3. Evaluation metrics for classification models in phase prediction.

Models	Accuracy (%)	Precision (%)	F1 score (%)	Recall (%)	ROC AUC (%)
Random Forest	**75**	**76**	**73**	**74**	**96**
Ensemble	**77**	**78**	**76**	**76**	**97**

Table 4 presents the phase prediction results obtained from the random forest model and the ensemble model. For each prediction, the two highest probability values predicted by each model were recorded to analyze the effects on subcategories under high secondary phase interference conditions. Both models successfully predict the same primary phases; however, the secondary phases differ. These differences are associated with possible equilibrium conditions at varying temperatures, which must be validated through phase diagrams generated via CALPHAD. Analyzing the VEC parameters reveals that, according to Oñate et al. [35], the AlCrFeMnNi alloy would exhibit a stable BCC+IM phase ($5.59 \leq VEC \leq 7.28$), suggesting the presence of the B2 phase. Phase stability based on VEC was also discussed by Ma et al. [36], supporting the predominant presence of the BCC/B2 phase for VEC values below 7.4 in AlxNiCoFeCr compositional systems. Based on these findings and considering the objective of this study to achieve FCC+BCC+IM phases, only the AlCrFe2MnNi2 and AlCrFe2Ni2 alloys initially meet this condition.

Table 4. Phase prediction results obtained by the best machine learning models evaluated.

Alloy	Random Forest Prediction	Ensemble Prediction
CrFeMnNi	FCC (45.16%) FCC+BCC (21.08%)	FCC (40.3%) FCC+BCC (25.9%)
Cr2Fe2MnNi	FCC+BCC (51.17%) BCC (18.78%)	FCC+BCC (73%) FCC+BCC+IM (18%)
CrFe2MnNi2	FCC (82.46%) FCC+IM (13.84%)	FCC (83.9%) FCC+IM (12.2%)
AlCrFeMnNi	BCC (48.3%)	BCC (44.5%)

	FCC+BCC+IM (21.07%)	FCC+BCC+IM (26.3%)
AlCrFe2MnNi2	FCC+BCC (73.79%) BCC (8.63%)	FCC+BCC (68%) FCC+BCC+IM (12.8%)
AlCrFe2Ni2	FCC+BCC (43.12%) FCC+IM (21.26%)	FCC+BCC (42.83%) FCC+BCC+IM (13.51%)

The challenge in distinguishing the B2 phase from the BCC phase is evident in the machine learning results, where significant difficulty arises in predicting the FCC+BCC+IM phase. This is due to the high affinity between the BCC and B2 phases, whose characteristics and influence on predictive parameters differ from those generated by other intermetallics studied, such as the σ, μ, $L1_2$, or Laves phases. Similarly, the identification of predictive parameters for the B2 phase currently remains limited. Liu et al. [25] reported that the B2 phase is stable for VEC values between 6 and 7, which could be useful for phases that are stable within this range. However, this approach only accounts for the BCC phase and excludes the FCC+BCC and FCC phases, making it impractical for the functional design of multicomponent alloys requiring this intermetallic. The authors found no further studies to identify parameters for predicting the B2 phase in multicomponent alloys, a conclusion supported by Cabrera et al. [37]. The results of the exploratory data analysis of multicomponent alloys containing the B2 phase are shown in Figure 5. Figure 5(a) shows that δr and ΔHmix are not significant factors for predicting the B2 phase in BCC systems due to the high degree of overlap between these parameters for both phases (BCC and BCC+B2). However, VEC enables an accurate prediction of the B2 phase in BCC systems, as BCC+B2 is stable for VEC > 6.4 (see Figure 5(b)).

The stability of the B2 phase in FCC systems is depicted in Figure 5(c). It can be observed that the parameter enabling the prediction of the B2 phase in FCC systems is the atomic radius difference, with the FCC phase being stable for $\delta r < 5.23$ and the FCC+B2 phase being stable for $\delta r > 5.23$. In contrast, VEC does not allow for predicting the B2 phase in FCC systems due to the overlap in the valence electron concentration between FCC+B2 and FCC. This finding supports the notion that VEC

cannot be considered an absolute descriptor for all systems, as suggested by Liu et al. [25]. Consequently, this study provides clear predictive pathways for the proper design of alloys with B2 reinforcement mechanisms.

Figures 5(e) and 5(f) show that VEC, ΔHmix, and δr cannot predict the B2 phase in FCC+BCC systems due to the balance between the various parameters, leading to significant overlap. This finding clarifies and supports the machine learning results for B2 in predicting FCC+BCC+IM phases, indicating that an additional parameter is required to accurately predict the B2 phase in FCC+BCC systems. This is attributed to the affinity between the BCC and B2 phases, combined with the presence of the FCC phase, which creates a balance that reduces the effectiveness of the packing factor proposed in [35,38], as a descriptor for predicting intermetallics in multicomponent alloys, rendering it ineffective for predicting the B2 phase in this system.

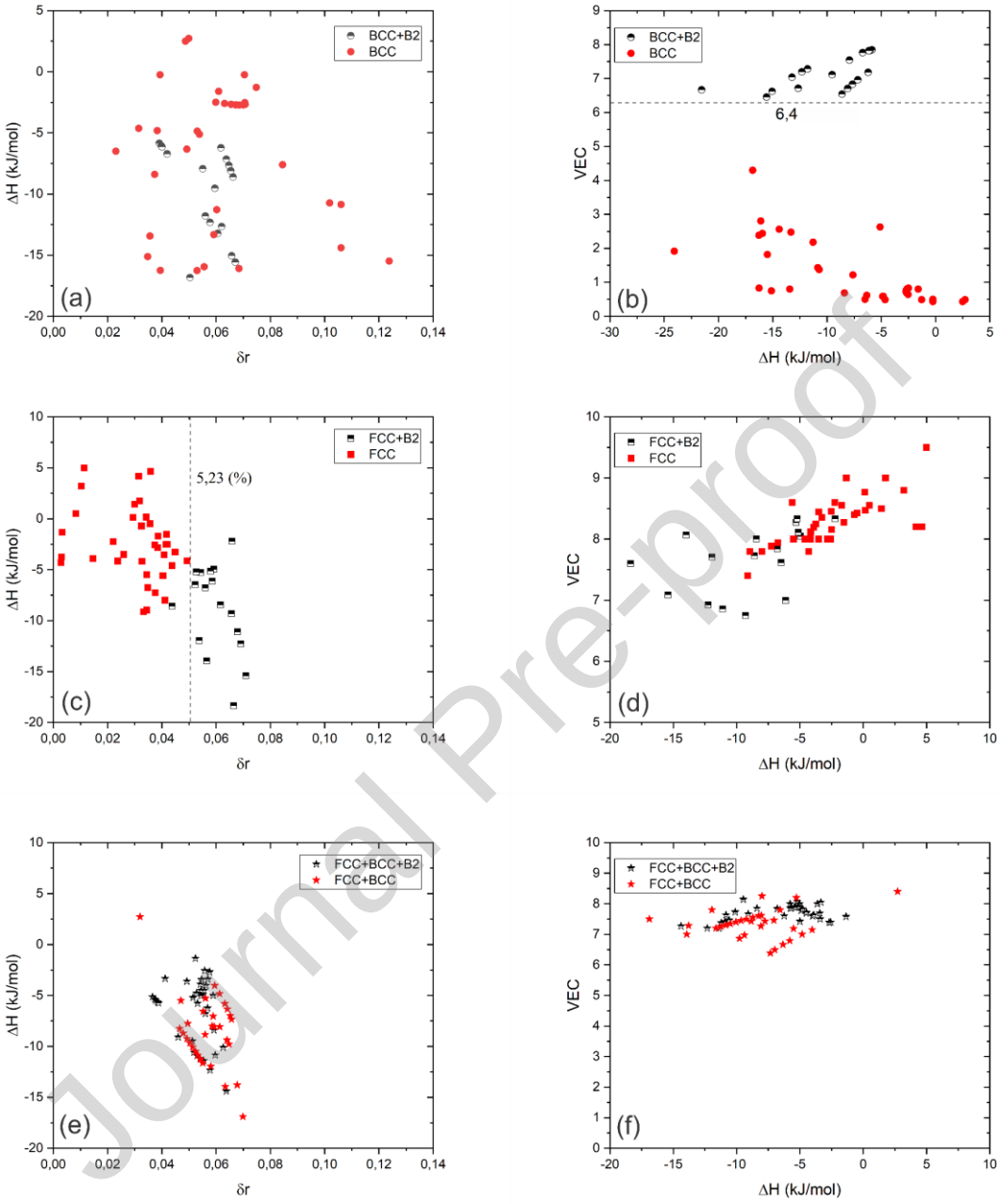

Figure 5. Exploratory Data Analysis in Systems with B2 Phase: (a) ΔHmix vs. δr in BCC and BCC+B2; (b) VEC vs. ΔHmix in BCC and BCC+B2; (c) ΔHmix vs. δr in FCC and FCC+B2; (d) VEC vs. ΔHmix in FCC and FCC+B2; (e) ΔHmix vs. δr in FCC+BCC and FCC+BCC+B2; (f) VEC vs. ΔHmix in FCC+BCC and FCC+BCC+B2

One of the factors influenced by intermetallics in multicomponent alloys, beyond the physicochemical affinity between intermetallics and the primary phases—such as the interaction between the B2 phase and the BCC phase—is the set of mechanical properties. However, these

mechanical properties are strongly related to the compositional system of the alloy, which could limit their use as predictors in multicomponent alloys.

To address this limitation, the shear modulus (G) was evaluated as a potential predictor in multicomponent alloys with compositional systems containing aluminum. This is because the shear modulus is directly related to slip resistance, a characteristic imparted by intermetallic phases such as B2 within the material. The correlation between G and δr is presented in Figure 6, where multicomponent alloys with aluminum exhibit the B2 phase in FCC+BCC systems for G>68.22 GPa. Based on these findings, the shear modulus can be effectively used as a predictor for the presence of the B2 phase in FCC+BCC systems for aluminum-based multicomponent alloys.

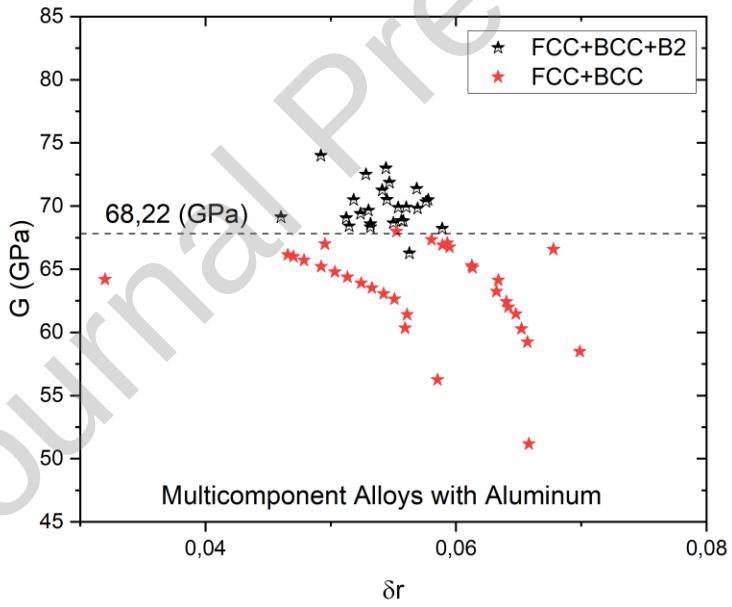

Figure 6. Exploratory Data Analysis in FCC+BCC Systems for Predicting B2 Using G vs. δr

Based on the results obtained from the exploratory data analysis, the machine learning predictions for the aluminum-containing alloys under study can be corrected. This adjustment yields the prediction results presented in Table 5 and Figure 7, which indicate that all the multicomponent alloys analyzed containing aluminum exhibit the B2 phase.

Table 5. Phase prediction results obtained by the best machine learning (ML) Model, corrected with the analytical predictive parameters derived in this study for the B2 phase.

Alloy	ML prediction model	ML prediction model with analytically predictive parameters
AlCrFeMnNi	BCC (48.30 %)	BCC+B2 (72.65 %)
AlCrFe2MnNi2	FCC+BCC (73.79%)	FCC+BCC+B2 (64.44 %)
AlCrFe2Ni2	FCC+BCC (43.12%)	FCC+BCC+B2 (60.041 %)

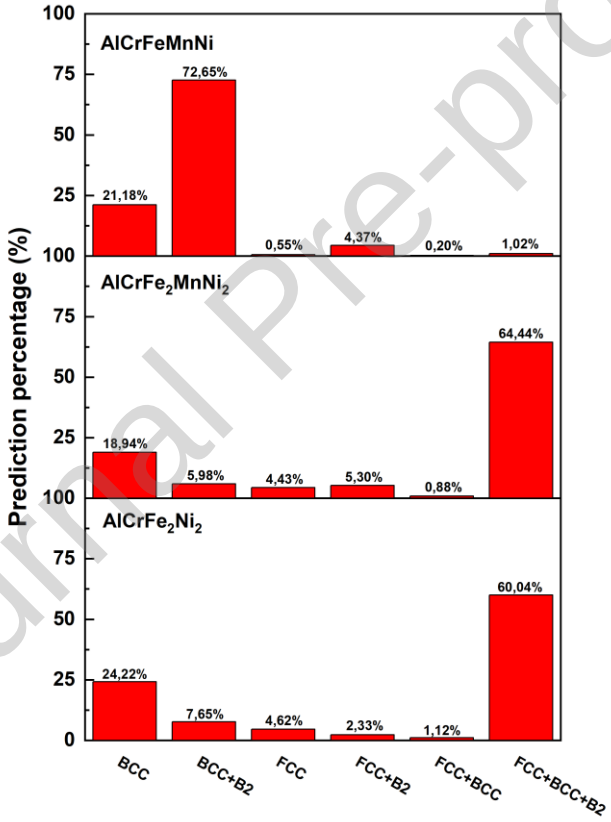

Figure 7. Probability distribution for phase prediction in the studied multicomponent alloys containing Al.

Figure 8 shows the phase stability of the alloys predicted using CALPHAD via Thermo-Calc. The results are consistent with those in Table 4 for machine learning predictions and Table 5 for machine learning predictions, corrected with the analytical predictive parameters derived from this study for the B2 phase. For the CrFe2MnNi2 alloy, a notably wide FCC compositional field is observed (see

Figure 8.c), supporting the machine learning prediction shown in Table 4. Similarly, for the AlCrFeMnNi alloy, Figure 8.d reveals phase stability in the BCC/B2 region between 600–980°C, while the predominant stability transitions to FCC+BCC/B2 above and below this temperature range. This finding is consistent with the competitive precision percentages obtained through machine learning predictions for the primary and secondary phases. Although the B2 phase was not explicitly predicted as the primary phase, its significant affinity with the disordered BCC phase highlights the complexity of its prediction. All the predicted phases are stable within a defined temperature range of 850°C–900°C according to CALPHAD thermodynamic equilibrium. This coherence is attributed to the constant cooling rate applied to all samples, ensuring that the equilibrium condition achieved during heat extraction is consistent within a similar temperature range.

Overlap between the B2 and BCC phases has been observed across various methods because of their high affinity. This is highlighted in the work of Calvo et al. [39], who established that mixed phases occur within the e/a range of 1.65 to 2.05, while the BCC phase is observed for values exceeding 2.05. When these parameters are compared with those obtained for each evaluated alloy, all the values fall within the mixed-phase range. This is supported by the CALPHAD simulation results, as they indicate the stability of mixed phases at temperatures ranging between 700 and 800 (°C) (see Figure 8). However, the alloys that exhibit the B2 phase according to the phase diagrams are AlCrFeMnNi, AlCrFe2MnNi2, and AlCrFe2Ni2. Notably, the e/a values calculated for these alloys (see Table 1) are the highest, with values of 2.0, 2.0, and 2.17, respectively, justifying the presence of the B2 phase. This is because the B2 phase, being an ordered intermetallic phase, is influenced by greater electronic stabilization, which is favored by a compositional electronic configuration that promotes regular atomic ordering within the stable lattice. Furthermore, as observed in Table 5, after the machine learning results are corrected with the newly derived analytical predictive parameters from this study, the B2 phase is found in all the evaluated aluminum-containing alloys. This finding is supported by the CALPHAD results.

Poletti et al. [40] established that intermetallic phases tend to form at e/a values lower than those required for the BCC phase (> 2,05). However, they did not discuss how electronic concentration values vary for FCC+BCC+IM, FCC+IM, or BCC+IM systems, making it likely that the analyzed BCC values are influenced by the B2 phase. Additionally, in the group of FCC+BCC+IM phases analyzed, consisting of 15 alloys, only the sigma and Laves phases were identified as intermetallics.

The work of Toda-Caraballo et al. [41], demonstrated that FCC+BCC+IM classifications can occupy a higher e/a concentration range compared to the FCC+BCC group. Similarly, the BCC+IM phase shows a tendency to appear in the lower or central e/a concentration range relative to the BCC group. A detailed analysis of the work by Toda-Caraballo et al. [41], although not explicitly mentioned in the document or clearly detailed, reveals that the FCC+BCC+IM phase is observed at e/a values between 1.8 and 2.1, while the FCC+BCC phase is found at e/a values between 1.6 and 1.9. This finding verifies the increase in the electronic concentration of the BCC phase caused by contributions from phases such as B2, confirming the results obtained in this study. Moreover, it is important to consider conducting e/a comparisons within the same compositional systems to accurately determine the increase or decrease in e/a when intermetallic phases are present.

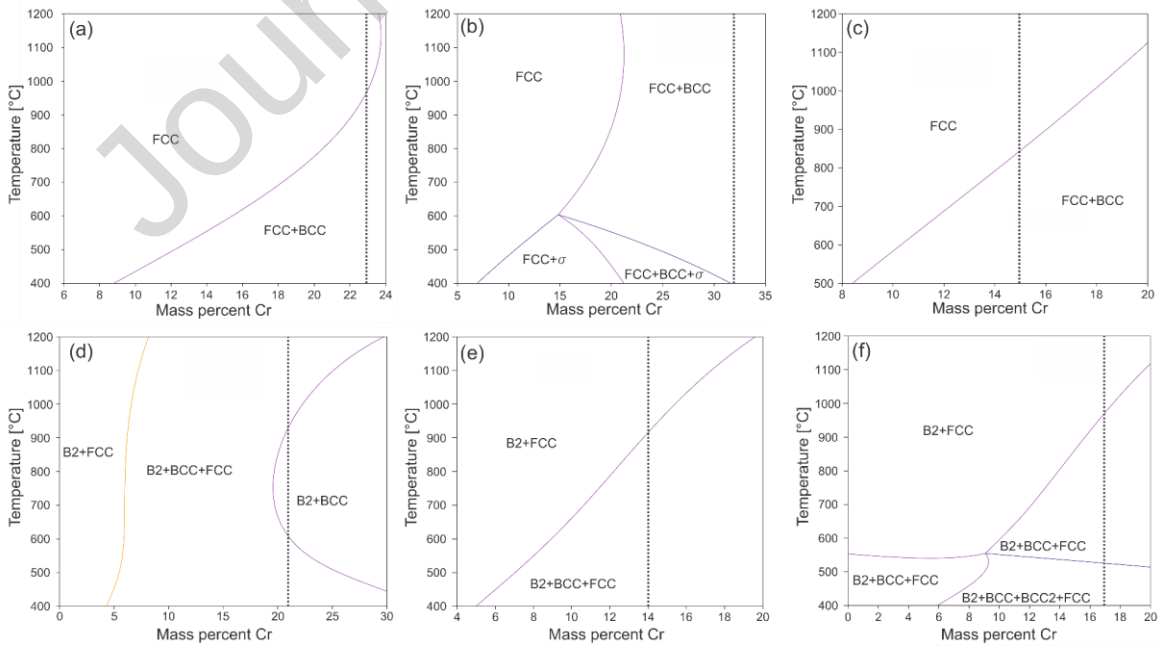

Figure 8. Phase diagrams for each analyzed alloy: (a) CrFeMnNi; (b) Cr2Fe2MnNi; (c) CrFe2MnNi2; (d) AlCrFeMnNi; (e) AlCrFe2MnNi2; (f) AlCrFe2Ni2.

3.2. DTA characterization

Figure 9 presents the cooling curves obtained through DTA. The reactions occurring during cooling are characterized by exothermic peaks. The peaks observed in the curves for the aluminum-free samples are consistent with the results obtained through machine learning and CALPHAD, validating the predicted outcomes. However, for the group of aluminum-containing samples, CALPHAD demonstrated a high predictive capacity for phase identification when analyzing broad ranges of thermodynamic stability. In contrast, the machine learning models encounter challenges in accurately predicting complex phases with high affinity. Moreover, this limitation was addressed by incorporating newly derived analytical parameters for the B2 phase in the FCC, BCC, and FCC+BCC systems, enabling a more efficient alloy design for applications requiring the B2 phase.

An example of this is the AlCrFeMnNi alloy. CALPHAD indicates the presence of BCC/B2 phases between approximately 600°C and 940°C, whereas machine learning predicts a higher likelihood for the BCC phase without intermetallics (IM). Nevertheless, when analyzing the second most probable phase prediction in the machine learning models for the AlCrFeMnNi alloy, both the random forest and ensemble models predict FCC+BCC+IM. These results are consistent with the CALPHAD analysis (Figure 8.d) for temperatures above 940°C.

In the case of the $AlCrFe_2MnNi_2$ and $AlCrFe_2Ni_2$ alloys, both exhibit the B2+FCC phase above 900°C and 1000°C, respectively. This is supported by machine learning predictions for both alloys, which indicate FCC+BCC. These findings corroborate that, owing to the high affinity of the BCC/B2 phase, accurately identifying this intermetallic phase via machine learning is challenging unless an efficient predictor is developed to achieve better classification with the implemented model.

When examining the DTA curves in Figure 9.b for the aluminum-containing alloys, the formation of a BCC/B2 structure is observed in the AlCrFeMnNi alloy, while FCC+BCC/B2 structures are

observed in the $AlCrFe_2MnNi_2$ and $AlCrFe_2Ni_2$ alloys. DTA analysis cannot precisely identify the formation of the B2 phase; hence, it is considered as possible coexistence, indicated as BCC/B2. However, the CALPHAD results and the two most significant phase probabilities from the ensemble machine learning model suggest a high likelihood of B2 phase presence, which is supported by the thermodynamic stability predicted by CALPHAD.

Based on these findings, the alloys of interest for this study will focus on those containing aluminum, specifically those exhibiting FCC+BCC/B2 phases. These include the AlCrFe2MnNi2 and AlCrFe2Ni2 alloys. It should be noted that although the cooling rate used was 5°C/min, which can be considered close to equilibrium conditions, discrepancies with thermodynamic simulations may arise due to the kinetics and varying diffusion rates of the elements constituting the compositional system, resulting in quasi-equilibrium conditions. For this reason, the resulting microstructures of these alloys must be carefully analyzed.

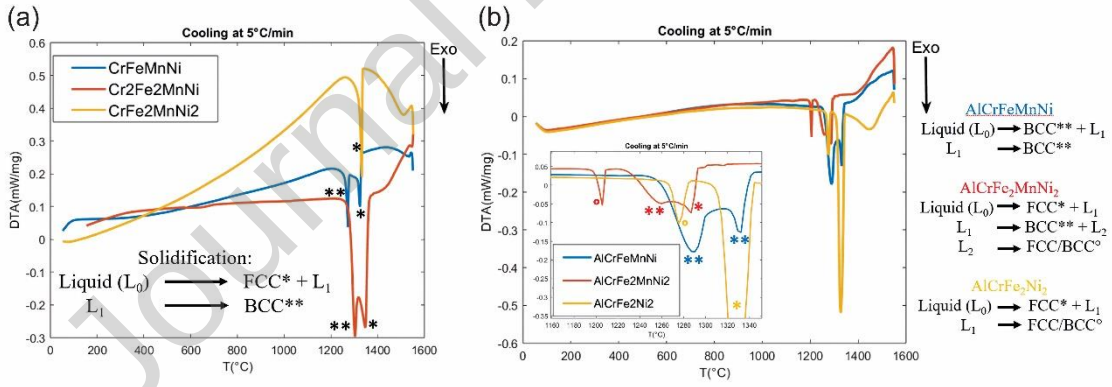

Figure 9. Differential thermal analysis results: (a) samples without aluminum content; (b) samples with aluminum content.

3.3. Microstructural characterization

Figure 10 displays a backscattered electron SEM micrograph. Figure 10(a) shows the microstructural characterization results for the AlCrFe2MnNi2 alloy, revealing a structure with elongated grains and interdendritic phases featuring cellular or globular structures. This microstructure consists of

FCC+BCC/B2 phases, as determined by microstructural characterization and CALPHAD simulation results. Additionally, Figure 10(b) demonstrates the presence of a homogeneous distribution of phases within the microstructure. Figure 10(c) shows the microstructure of the AlCrFe2Ni2 alloy, which also exhibited FCC+BCC/B2 phases. Figure 10(d) highlights well-defined phase domains, including dendritic and interdendritic regions. Figure 10(e) shows that the AlCrFeMnNi alloy is composed of BCC/B2 phases. Figure 10(f) shows a primary matrix with spinodal decomposition zones, characteristic of BCC/B2 phase transformations in multicomponent alloys. Although VEC theory predicts that the equimolar AlCrFeMnNi sample should form a single-phase solid solution, Figure 10(c) reveals a transformation occurring between 1340°C and 1240°C, with no further solidification transformations at lower temperatures, since solid-state transformation, such as spinodal decomposition, cannot be observed via DTA. According to previous studies, the dendritic regions are characterized by an FCC+B2 mixed matrix rich in Cr and Fe, containing cubic precipitates enriched in Al and Ni. Conversely, the interdendritic regions feature a BCC matrix rich in Al and Ni embedded with elongated, rod-like precipitates rich in Cr and Fe belonging to the B2 phase.

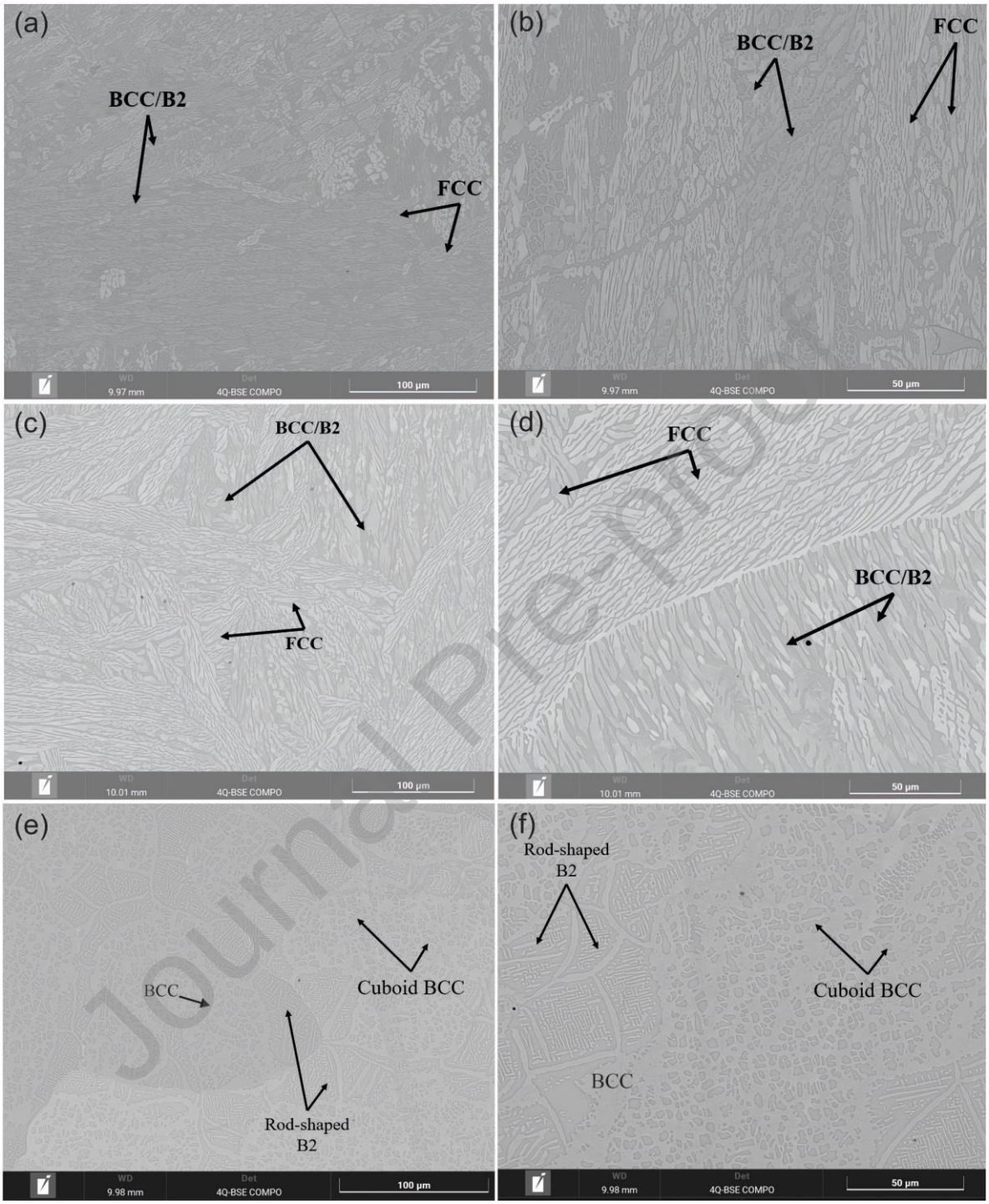

Figure 10. SEM microstructural characterization results for multicomponent alloys containing Al: (a) AlCrFe2MnNi2 at 1000x magnification; (b) AlCrFe2MnNi2 at 2000x magnification; (c) AlCrFe2Ni2 at 1000x magnification; (d) AlCrFe2Ni2 at 2000x magnification; (e) AlCrFeMnNi at 1000x magnification; (f) AlCrFeMnNi at 2000x magnification.

The results in Figure 11 demonstrate the presence of FCC+BCC/B2 phases in the AlCrFe2MnNi2 alloy, where the eutectic lamellar structure with an interdendritic zone featuring a cellular or globular structure is observed (see Figure 11(a)). Additionally, Figure 11(b) presents the EBSD analysis, which provides detailed evidence of the FCC+BCC/B2 phases in the alloy, thereby validating the computational phase prediction results.

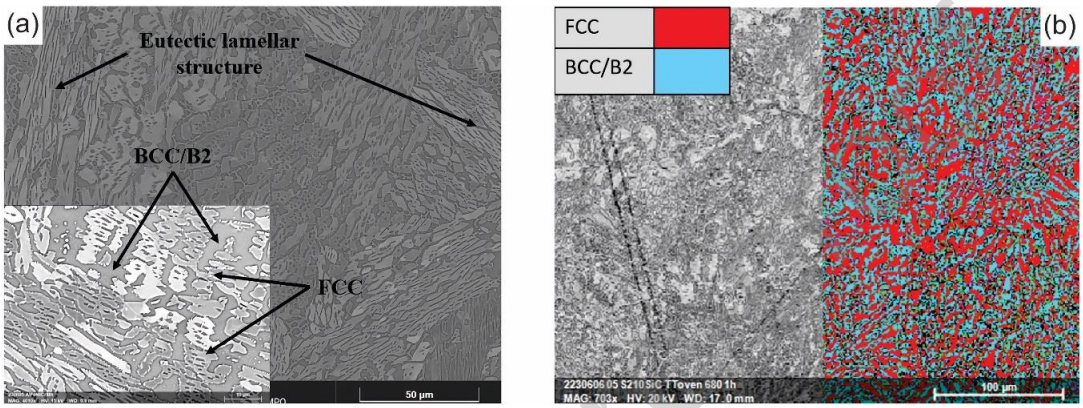

Figure 11. SEM-EBSD microstructural characterization results for the AlCrFe2MnNi2 alloy: (a) SEM image showing FCC and BCC/B2 structures; (b) phase identification analysis via EBSD.

The detailed microstructure of the AlCrFe2Ni2 alloy is shown in Figure 12. It exhibits an FCC and BCC/B2 phase with a lamellar eutectic structure and well-defined domains (Figure 12(a)). Additionally, the BCC/B2 phase, as in the AlCrFe2MnNi2 alloy, is observed within the alloy matrix. Figure 12(b) clearly illustrates the eutectic microstructure composed of FCC and BCC/B2 phases through EBSD analysis.

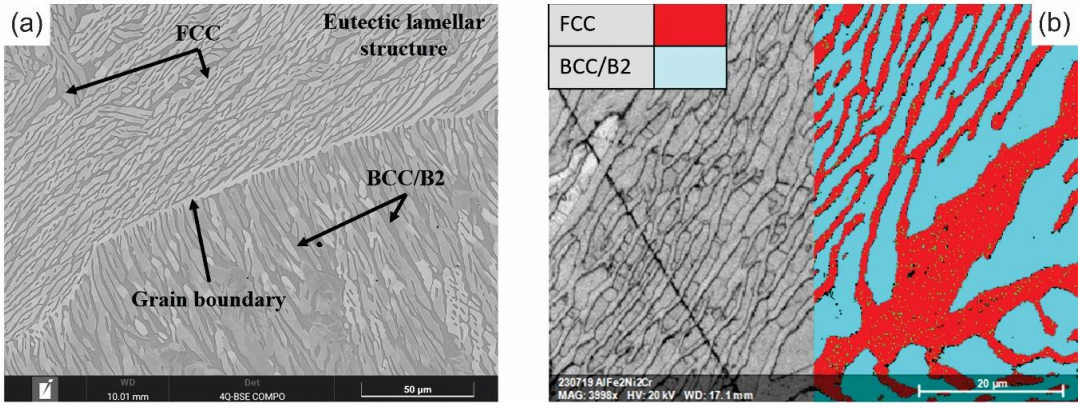

Figure 12. SEM-EBSD microstructural characterization results for the AlCrFe2Ni2 alloy: (a) SEM image showing FCC and BCC/B2 structures; (b) Phase identification analysis using EBSD.

The results demonstrated that combining random forest and XGBoost models with an ensemble approach optimized for parameter tuning enhances the prediction accuracy of complex phases with high overlap, such as the FCC+BCC+IM phase. Moreover, the incorporation of new key parameters for predicting the B2 phase in multicomponent systems has allowed for a more comprehensive prediction of the intermetallic B2 phase, introducing three new parameters for its identification in FCC, BCC, and FCC+BCC systems. This advancement overcomes previous limitations in phase prediction, enabling the design of multicomponent alloys with the strengthening mechanism of an ordered BCC phase.

These findings significantly improve the design capabilities of advanced multicomponent alloys, facilitating the balance between strength and ductility through the incorporation of the B2 phase as a reinforcing agent. Additionally, these results open new research opportunities to further integrate the analytical parameters obtained in this study into machine learning systems, thereby further optimizing phase prediction. Unfortunately, achieving a fully integrated predictive system requires a larger dataset, emphasizing the need for expanded experimental and computational data to increase model accuracy and reliability.

4. Conclusion

The optimization of FCC+BCC+IM phase prediction was separately investigated using an ensemble methodology with parametric optimization through supervised machine learning on a robust database, while the identification of the B2 phase was analyzed through new analytical predictive parameters and validated via CALPHAD simulations and experimental results. The key findings indicate the following:

1. The ensemble method with parametric optimization between random forest and XGBoost achieved 77% accuracy in multiclass phase classification, improving the identification of highly overlapping complex phases, such as FCC+BCC+IM, from 25% to 62.5%.
2. The valence electron concentration was identified as a critical primary predictor, highlighting its global influence on phase prediction. However, it does not overcome the challenges of predicting high-entropy ordered intermetallic phases, such as the B2 phase, which requires additional predictive parameters to increase accuracy.
3. Three new predictive parameters for the B2 phase in multicomponent alloys were established for FCC, BCC, and FCC+BCC systems, demonstrating that VEC alone is insufficient to predict this intermetallic phase in multicomponent systems. The new analytical predictive parameters indicate the following:
    a. The B2 phase is stable in FCC systems if $\delta r > 5.23\%$.
    b. The B2 phase is stable in BCC systems if $VEC > 6.4$.
    c. The B2 phase is stable in FCC+BCC systems if $G > 68.22$ GPa.

    These new parameters establish effective design pathways for functional multicomponent alloys and open avenues for future optimization of phase prediction through multiclass machine learning models focusing on high-entropy ordered intermetallics.
4. CALPHAD simulations and experimental results validate the findings obtained through the ensemble machine learning method with parametric optimization, complementing the newly derived analytical predictive parameters for the B2 phase established in this study.

Data availability

The data used in this research are available upon request.

Author contributions statement

Angelo Oñate: Investigation, Methodology, Visualization, Data curation, Formal analysis, Writing – original draft, Review & editing, Herrim Seidou: Resources, Investigation, Data curation, Methodology, Review & editing; Jérome Tchoufang-Tchuindjang: Review & editing; Víctor Tuninetti: Resources; Visualization, Review & editing; Alejandra Miranda: Review & editing; Juan Pablo Sanhueza: Resources, Review & editing; Anne Mertens: Resources, Methodology, Investigation; Review & editing

Declaration of competing interest

The authors declare that they have no known competing financial interests or personal relationships that could have appeared to influence the work reported in this paper.

References

[1] M. Zhang, C. Luo, G. Zhang, H. Xu, G. Li, Machine learning-assisted discovery of phase transformed Al-Ni co-doping high entropy alloys for superior corrosion resistance, J Alloys Compd 1006 (2024) 176354. https://doi.org/10.1016/j.jallcom.2024.176354.

[2] J. Liu, Z. Li, D. Lin, Z. Tang, X. Song, P. He, S. Zhang, H. Bian, W. Fu, Y. Song, Eutectic high-entropy alloys and their applications in materials processing engineering: A review, J Mater Sci Technol 189 (2024) 211–246. https://doi.org/10.1016/j.jmst.2023.10.057.

[3] Y. Lu, Y. Dong, H. Jiang, Z. Wang, Z. Cao, S. Guo, T. Wang, T. Li, P.K. Liaw, Promising properties and future trend of eutectic high entropy alloys, Scr Mater 187 (2020) 202–209. https://doi.org/10.1016/j.scriptamat.2020.06.022.

[4] Y. Zhou, Z. Zhang, D. Wang, W. Xiao, J. Ju, S. Liu, B. Xiao, M. Yan, T. Yang, New trends in additive manufacturing of high-entropy alloys and alloy design by machine learning: from single-phase to multiphase systems, Journal of Materials Informatics 2 (2022) 18. https://doi.org/10.20517/jmi.2022.27.

[5] X. Lin, Y. Liu, Q. He, P. Huang, W. Wu, J. Zhang, W. Peng, Q. Guo, Exploring the La microalloying effects on the electrochemical properties of AlCoCrFeNi2.1 EHEAs in simulated PEMFC environments, J Alloys Compd 1010 (2025) 177879. https://doi.org/10.1016/j.jallcom.2024.177879.

[6] S. Shuang, Z.Y. Ding, D. Chung, S.Q. Shi, Y. Yang, Corrosion resistant nanostructured eutectic high entropy alloy, Corros Sci 164 (2020). https://doi.org/10.1016/j.corsci.2019.108315.

[7] Z.J. Shi, Z.B. Wang, X.D. Wang, S. Zhang, Y.G. Zheng, Effect of thermally induced B2 phase on the corrosion behavior of an Al0.3CoCrFeNi high entropy alloy, J Alloys Compd 903 (2022). https://doi.org/10.1016/j.jallcom.2022.163886.

[8] L. Song, W. Hu, X. Zhang, B. Liao, S. Wan, L. Kang, X. Guo, Corrosion Behavior of the AlCoCrFeNi2.1 Eutectic High-Entropy Alloy in Chloride-Containing Sulfuric Acid Solutions at Different Temperatures, Materials 15 (2022). https://doi.org/10.3390/ma15144822.

[9] H. Wu, J. Xie, H.-Y. Yang, D.-L. Shu, G.-C. Hou, J.-G. Li, Y.-Z. Zhou, X.-F. Sun, Comparative Study of Mechanical and Corrosion Behaviors of Cost-Effective AlCrFeNi High Entropy Alloys, J Mater Eng Perform 31 (2022) 4472–4482. https://doi.org/10.1007/s11665-021-06563-w.

[10] H. Zhang, H. Huang, C. Wang, H. Zhang, H. Wu, H. Zhao, Nanoindentation behaviors of the AlCoCrFeNi2.1 eutectic high-entropy alloy: The effects of crystal structures, J Alloys Compd 1008 (2024) 176535. https://doi.org/10.1016/j.jallcom.2024.176535.

[11] A.D. Pope, S. Iwan, M.P. Clay, J. Ren, W. Yang, W. Chen, Y.K. Vohra, Phase stability of a eutectic high entropy alloy under extremes of pressures and temperatures, AIP Adv 14 (2024). https://doi.org/10.1063/5.0188644.

[12] H. Jiang, Z. Ni, S. Lu, H. Li, Y. Li, Y. Dong, Effect of remelting and heat treatment on the microstructure and mechanical properties AlCoCrFeNi2.1 eutectic high entropy alloy, J Alloys Compd (2025) 179360. https://doi.org/10.1016/j.jallcom.2025.179360.

[13] Q. Zhang, Z. Chen, Y. Dong, C. Li, Y. Wang, High strength and ductility eutectic high entropy alloy with unique core-shell structure, J Alloys Compd 976 (2024) 173141. https://doi.org/10.1016/j.jallcom.2023.173141.

[14] Y.-G. Yan, D. Lu, K. Wang, Overview: recent studies of machine learning in phase prediction of high entropy alloys, Tungsten 5 (2023) 32–49. https://doi.org/10.1007/s42864-022-00175-0.

[15] S. Liu, B. Bocklund, J. Diffenderfer, S. Chaganti, B. Kailkhura, S.K. McCall, B. Gallagher, A. Perron, J.T. McKeown, A comparative study of predicting high entropy alloy phase fractions with traditional machine learning and deep neural networks, NPJ Comput Mater 10 (2024) 172. https://doi.org/10.1038/s41524-024-01335-1.

[16] A. Choudhury, S. Kumar, Breaking data barriers: advancing phase prediction in high entropy alloys through a new machine learning framework, Canadian Metallurgical Quarterly (2024) 1–11. https://doi.org/10.1080/00084433.2024.2395674.

[17] A. Bansal, P. Kumar, S. Yadav, V.S. Hariharan, R. M R, G. Phanikumar, Accelerated design of high entropy alloys by integrating high throughput calculation and machine learning, J Alloys Compd 960 (2023) 170543. https://doi.org/10.1016/j.jallcom.2023.170543.

[18] L. Zhinchao, M. Dong, L. Xiongjun, Z. Lu, High-throughput and data-driven machine learning techniques for discovering high-entropy alloys, Commun Mater 5 (2024) 1–19.

[19] I. Peivaste, E. Jossou, A.A. Tiamiyu, Data-driven analysis and prediction of stable phases for high-entropy alloy design, Scientific Reports 2023 13:1 13 (2023) 1–21. https://doi.org/10.1038/s41598-023-50044-0.

[20] J. He, Z. Li, P. Zhao, H. Zhang, F. Zhang, L. Wang, X. Cheng, Machine learning-assisted design of high-entropy alloys with superior mechanical properties, Journal of Materials Research and Technology 33 (2024) 260–286. https://doi.org/10.1016/j.jmrt.2024.09.014.

[21] Y. Yan, X. Hu, Y. Liao, Y. Zhou, W. He, T. Zhou, Recent machine learning-driven investigations into high entropy alloys: A comprehensive review, J Alloys Compd 1010 (2025) 177823. https://doi.org/10.1016/j.jallcom.2024.177823.

[22] S. Hou, Y. Li, M. Bai, M. Sun, W. Liu, C. Wang, H. Tetik, D. Lin, Phase Prediction of High-Entropy Alloys by Integrating Criterion and Machine Learning Recommendation Method, Materials 15 (2022) 3321. https://doi.org/10.3390/ma15093321.

[23] X. Liu, J. Zhang, Z. Pei, Machine learning for high-entropy alloys: Progress, challenges and opportunities, Prog Mater Sci 131 (2023) 101018. https://doi.org/10.1016/J.PMATSCI.2022.101018.

[24] S. Li, R. Liu, H. Yan, Z. Li, Y. Li, X. Li, Y. Zhang, B. Xiong, Machine Learning Phase Prediction of Light-Weight High-Entropy Alloys Containing Aluminum, Magnesium, and Lithium, Metals (Basel) 14 (2024) 400. https://doi.org/10.3390/met14040400.

[25] Z. Liu, L. Zhang, Phase formation criteria for structurally ordered high-entropy intermetallics, J Alloys Compd 981 (2024) 173716. https://doi.org/10.1016/J.JALLCOM.2024.173716.

[26] C. Wang, W. Zhong, J.-C. Zhao, Insights on phase formation from thermodynamic calculations and machine learning of 2436 experimentally measured high entropy alloys, J Alloys Compd 915 (2022) 165173. https://doi.org/10.1016/j.jallcom.2022.165173.

[27] Z.Q. Chen, Y.H. Shang, X.D. Liu, Y. Yang, Accelerated discovery of eutectic compositionally complex alloys by generative machine learning, NPJ Comput Mater 10 (2024) 204. https://doi.org/10.1038/s41524-024-01385-5.

[28] A. Oñate, J.P. Sanhueza, D. Zegpi, V. Tuninetti, J. Ramirez, C. Medina, M. Melendrez, D. Rojas, Supervised machine learning-based multi-class phase prediction in high-entropy alloys using robust databases, J Alloys Compd 962 (2023) 171224. https://doi.org/10.1016/J.JALLCOM.2023.171224.

[29] C.E. Precker, A. Gregores Coto, S. Muíños Landín, Materials for Design Open Repository. High Entropy Alloys, (2021). https://doi.org/10.5281/ZENODO.6403257.

[30] R. Machaka, Dataset for High-Entropy Alloys Phases, 3 (2021). https://doi.org/10.17632/7FHWRGFH2S.3.

[31] A.H. SEIDOU, Differential thermal analysis to assist the design of corrosion-resistant high entropy alloys for laser powder bed fusion, in: 2024: pp. 353–362. https://doi.org/10.21741/9781644903131-40.

[32] L. Zhang, C.-S. Oh, Y.S. Choi, Improved phase prediction of high-entropy alloys assisted by imbalance learning, Mater Des 246 (2024) 113310. https://doi.org/10.1016/j.matdes.2024.113310.

[33] Z. Tang, S. Zhang, R. Cai, Q. Zhou, H. Wang, Designing High Entropy Alloys with Dual fcc and bcc Solid-Solution Phases: Structures and Mechanical Properties, Metallurgical and Materials Transactions A 50 (2019) 1888–1901. https://doi.org/10.1007/s11661-019-05131-1.

[34] Y. Zhang, W. Ren, W. Wang, S. Ding, N. Li, A New Phase Classifier with an Optimized Feature Set in ML-Based Phase Prediction of High-Entropy Alloys, Applied Sciences 13 (2023) 11327. https://doi.org/10.3390/app132011327.

[35] A. Oñate, J.P. Sanhueza, J. Ramirez, C. Medina, M.F. Melendrez, D. Rojas, Design of Fe36.29Cr28.9Ni26.15Cu4.17Ti1.67V2.48C0.46 HEA using a new criterion based on VEC: Microstructural study and multiscale mechanical response, Mater Today Commun 35 (2023) 105681. https://doi.org/10.1016/J.MTCOMM.2023.105681.

[36] Y. Ma, B. Jiang, C. Li, Q. Wang, C. Dong, P. Liaw, F. Xu, L. Sun, The BCC/B2 Morphologies in AlxNiCoFeCr High-Entropy Alloys, Metals (Basel) 7 (2017) 57. https://doi.org/10.3390/met7020057.

[37] M. Cabrera, Y. Oropesa, J.P. Sanhueza, V. Tuninetti, A. Oñate, Multicomponent alloys design and mechanical response: From high entropy alloys to complex concentrated alloys, Materials Science and Engineering: R: Reports 161 (2024) 100853. https://doi.org/10.1016/J.MSER.2024.100853.

[38] Z. Wang, Y. Huang, Y. Yang, J. Wang, C.T. Liu, Atomic-size effect and solid solubility of multicomponent alloys, Scr Mater 94 (2015) 28–31. https://doi.org/10.1016/J.SCRIPTAMAT.2014.09.010.

[39] M. Calvo-Dahlborg, S.G.R. Brown, Hume-Rothery for HEA classification and self-organizing map for phases and properties prediction, J Alloys Compd 724 (2017) 353–364. https://doi.org/10.1016/j.jallcom.2017.07.074.

[40] M.G. Poletti, L. Battezzati, Electronic and thermodynamic criteria for the occurrence of high entropy alloys in metallic systems, Acta Mater 75 (2014) 297–306. https://doi.org/10.1016/j.actamat.2014.04.033.

[41] I. Toda-Caraballo, P.E.J. Rivera-Díaz-del-Castillo, A criterion for the formation of high entropy alloys based on lattice distortion, Intermetallics (Barking) 71 (2016) 76–87. https://doi.org/10.1016/j.intermet.2015.12.011.

Highlights

- **B2 phase is stable in FCC when the atomic radius difference exceeds 5.23%**

- **B2 phase is stable in BCC when the VEC exceeds 6.4**
- **B2 phase is stable in FCC+BCC when the shear modulus exceeds 68 GPa**
- **New predictive framework for B2 phase in HEAs**